JOURNAL OF MAGNETIC RESONANCE 29, 355–373 (1978)

Biological and Medical Imaging by NMR

P. MANSFIELD AND I. L. PYKETT

Department of Physics, University of Nottingham, Nottingham, England

PRESENTED AT THE SIXTH INTERNATIONAL SYMPOSIUM ON MAGNETIC RESONANCE, BANFF, ALBERTA, CANADA, MAY 1977

Several methods of producing NMR images are discussed and examples of biological application are given. The discussion emphasizes spin density projections as an introduction to the new method of echo-planar imaging, which is fully described. An example showing the first picture produced by this method is presented. The problems of scaling up medical imaging experiments to whole-body size are also discussed and the type of image expected from such experiments is anticipated by constructing cross-sectional water content maps of a human subject.

INTRODUCTION

The study of macroscopic structure in biological materials cannot ordinarily be attempted with conventional NMR techniques because each piece of resonant material in a specimen is not uniquely defined magnetically. However, by applying linear magnetic field gradients plus suitable rf irradiation it is possible to uniquely assign fields, and hence frequencies, to all points in the specimen. The NMR signal coming from a localized region of the sample is directly related to the mobile spin density at that point. A regular array of such points is used to form a visual image of the object. By mobile spins we have in mind particularly the protons contained in the free or nearly free water, fat, or oil distributed throughout the soft tissue regions in a biological subject, although one could, with less sensitivity, observe other nuclei. Bone structures contain relatively few mobile protons but are nevertheless generally detectable through an absence of signal.

In this presentation a common theme is emphasized which runs through our various methods of NMR imaging from our first publication on the matter (*1*) to our current imaging methods, namely, discrete spin density projections. A number of other imaging techniques, based on somewhat different principles, are also under development (*2–5*).

The goal of all imaging methods is to produce good-quality spin density images in the most efficient and the most practical manner possible. There are many contributory factors in the evaluation of the various imaging techniques, but a comparison of their merits is beyond the scope of this paper. However, for those engaged in the daily practice of NMR imaging, one important criterion has emerged, namely, the speed at which a complete picture can be produced. Standing in some awkward stance with one's hand in the NMR probe for 20 min or so gives time for reflection on just how imaging can be speeded up without impairing signal/noise ratios.

0022–2364/78/0292–0355 $02.00/0

DOI of original item: doi: 10.1016/0022-2364(78)90159-2

Apart from discomfort, there are scientific reasons for imaging at high speed. In a living person, various organs and parts of the body undergo involuntary movements, that is to say, they are controlled by the autonomic nervous system. The obvious example is, of course, the rhythmic beat of the heart. The stomach also undergoes contractions of a less regular nature. Breathing, though controllable, affects the position of all the vital organs to varying degrees. Holding the breath obviates this movement but for the aged or infirm, holding the breath in excess of 20 sec or so might prove impossible.

Then there is the possibility of visualization and measurement of blood flow. This has a pulsatile component deriving from the ventricular diastole and systole occurring roughly once per second in a normal state. It would not seem unreasonable to assume that imaging methods capable of producing complete pictures in less than 1 sec might be adapted to blood flow measurement by triggering off suitable signals from an electrocardiogram, thus allowing signal averaging of the picture to be performed.

In this paper the principles of imaging are outlined particularly with reference to projections. Selective irradiation and how this may be used to produce pictures by line scanning is next discussed. The evolution from line scanning to the general class of planar and multiplanar imaging techniques is then described and the first example of an image produced by the new method of echo-planar imaging is presented.

Finally some of the problems of scaling up the hitherto small-object imaging experiments to whole-body size are briefly discussed. The type of picture from such experiments is anticipated by producing cross-sectional water distribution images based on measured water content in human tissue and observed cross-sectional anatomies of a human subject.

IMAGING PRINCIPLES

In conventional NMR spectrometers, one often makes a conscious effort to produce a static magnetic field $B_0\mathbf{i}$ as uniform as possible so that all spins in the sample experience the same field and hence precess at the same Larmor angular frequency ω_0 given by

$$\omega_0 = \gamma B_0, \qquad [1]$$

where γ is the magnetogyric ratio.

All imaging methods use magnetic field gradients of one type or another in addition to B_0 in order to impose spatial coordinates on the sample. That is to say, the position in the sample is converted into a frequency change by the relationship

$$\Delta\omega_x = \gamma G_x \Delta x, \qquad [2]$$

where the magnetic field gradient $G_x = \partial B_x/\partial x$. The field gradient is in general described by a tensor with nine components, but for large B_0 we need only be concerned with the three components $G_\alpha = \partial B_x/\partial\alpha$, where $\alpha = x, y, z$.

If we consider the resonance absorption lineshape of a sample of water contained in a rectangular-shaped cell and placed in one static gradient it is straightforward to see that when the gradient is normal to one surface of the cell, the absorption line will itself take on a rectangular profile.

The absorption profile is the spin density projection on an axis in the direction of the gradient **G**. If the sample is rotated through 45° with respect to the gradient direction, a new projection profile is obtained.

For simple geometrical shapes and homogeneous distributions of spins, it soon becomes obvious that a great deal concerning the cross-sectional shape of the object can be deduced from the one-dimensional projection profiles. For shapes with high symmetry, it is easy to see that the cross-sectional shape may be deduced from relatively few projections. In the case of a homogeneous cylinder or an annulus only one projection is required and one could visualize a system which recreates the two-dimensional disk or annulus image from such a single projection. A square also comes close to giving a single projection profile which could be used directly to produce a

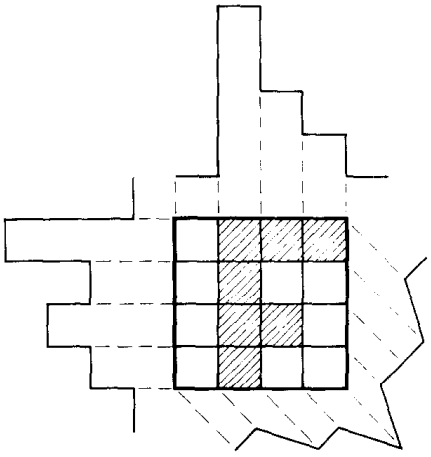

FIG. 1. Diagram showing three integrated spin density projections of an object in the shape of a letter F.

cross-sectional image. However, to be sure in this case, projections along two directions are required in order to eliminate a general rectangular shape or a diamond shape. Nevertheless, this line of enquiry leads one to ask whether there are any, more complicated, shapes which can be reconstructed from a single projection.

Let us imagine that our object lies within an image field which consists of a square matrix of sixteen touching elements as sketched in Fig. 1. Our image, the capital letter F, is represented in this array by the shaded squares which correspond to uniform spin density. The white squares represent zero spin density.

The spin density projections along the two principal axes and along a diagonal are sketched for this object. An interesting projection along the x axis gives the letter F (drawn here in reverse) directly although the y axis and diagonal projections do not of themselves reveal the cross-sectional form.

For a general irregular shape with varying spin density distribution, it is necessary to observe a number of projections of the object corresponding to regularly disposed orientations of the gradient. The two-dimensional distribution or image is then reconstructed from the set of projection data. A number of algorithms exist for executing this reconstruction (*6*, *7*). For a completely determined square matrix of m^2 elements, m separate projections are required. There are algorithms which can produce images from fewer projections but these are underdetermined systems and unless the

object has high symmetry they do not lead to a unique assignment of the matrix element densities.

The fact that certain shapes can give two-dimensional information from a single projection leads naturally to the question whether there is a particular projection direction which will always give the desired two-dimensional information. This does not seem to be the case for touching rectangular matrix elements. However, if we represent our matrix by discrete points then the image of the letter F appears as in Fig. 2. Again, the projections along the principal axes x and y are similar to the corresponding

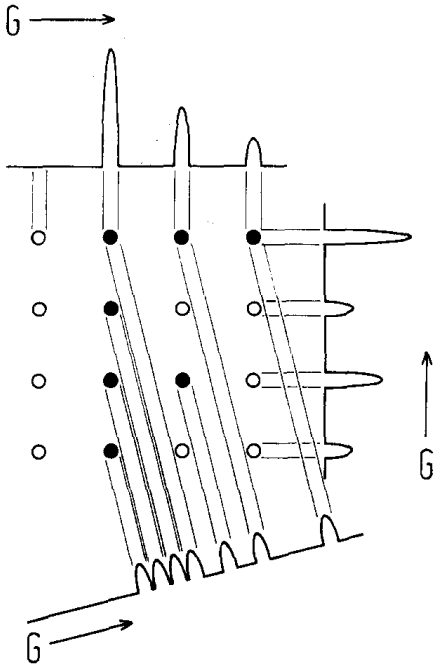

FIG. 2. Integrated density projections of a discrete array of spins forming a letter F. The open circles represent zero-density points.

projections in Fig. 1. But we notice for this discrete rectangular lattice that in addition there is a projection direction which simultaneously resolves *all* lattice points along one projection axis. Surprisingly, perhaps, a similar situation obtains for a three-dimensional lattice of discrete points.

We can understand these results better if we consider the transverse response or free induction decay (FID) for such a discrete lattice point distribution of spin density. For generality we consider an orthorhombic lattice with lattice constants a, b, c, in which resonant spins with density ρ_{lmn} reside at lattice points $x = la$, $y = mb$, and $z = nc$, where l, m, n are integers. If gradients G_x, G_y, and G_z are applied simultaneously along all three principal axes the FID following a 90° rf pulse is given by

$$S(t) = \text{r.p.} \sum_{l,m,n} \rho_{lmn} e^{i\gamma(laG_x + mbG_y + ncG_z)t} V, \qquad [3]$$

where V is the volume of spins contributing to the signal at each lattice site. The absorption lineshape is the Fourier transform of $S(t)$ and in general this will be a complicated stick spectrum with overlapping components. However, if we choose the

gradients in such a way as to satisfy the relationship

$$\Delta\omega_x/M = \Delta\omega_y = N\Delta\omega_z, \quad [4]$$

where

$$\Delta\omega_x = \gamma a G_x, \quad [5]$$

etc., and M, N are the largest values of m, n, respectively, in the imaging field, then all points in the Fourier-transformed spectrum are simultaneously resolved in a single calculation.

For a discrete lattice, then, this is the condition which ensures full two- or three-dimensional image resolution in a single FID. The problem is, of course, that spin systems do not come nicely packaged into discrete macroscopic lattices. Apart from regular or partially regular biological structures such as membranes and some fibrous tissues, there is little hope of applying the above ideas as a practical basis of imaging unless one can somehow *superimpose* a lattice structure on an otherwise continuous spin distribution. In later sections we shall return to this point, but for the moment we turn our attention to consider the characteristics of some biological tissues.

BIOLOGICAL TISSUE CHARACTERISTICS

Although NMR imaging will doubtless find applications in the study of plants and fluid transport, emphasis is placed here on the study of biological tissue in man. Biological tissue contains on average around 75% water, which can readily be detected by NMR methods. Quite a large fraction of the water is contained within the cell cytoplasm but there is also a substantial amount of extracellular water in addition to the bulk fluids contained within the body. Different healthy body tissues contain different amounts of water and the variation in water content can be used to some extent to differentiate the various organs within the body. Figure 3 shows the water content of various human tissues and apart from bone tissue, the total variation is rather small. Many factors affect water content so there can be considerable overlap of the distribution spreads for a given tissue type among different subjects. Nevertheless, one

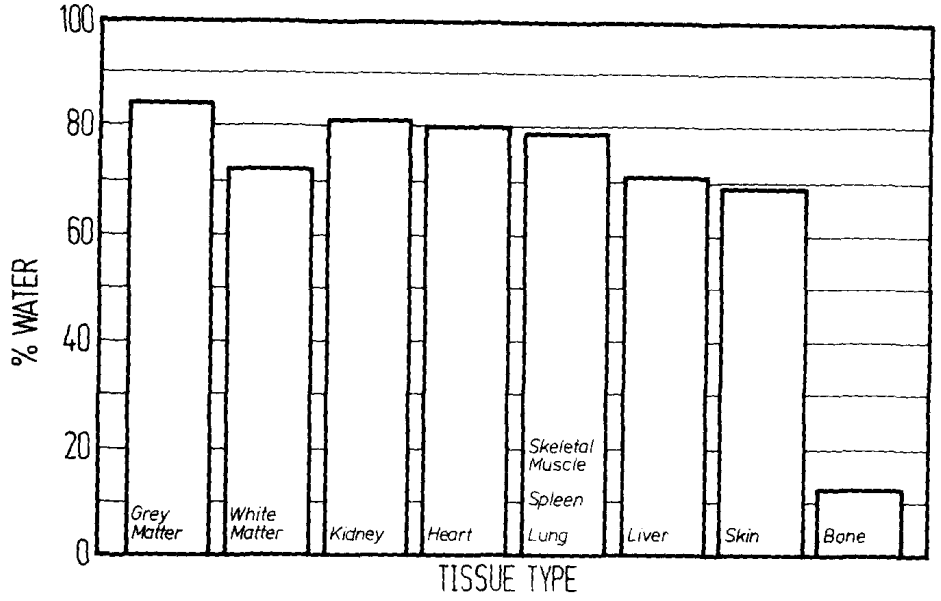

FIG. 3. Water content of various human tissues.

would certainly expect a variation in water content among the various organs and tissues in a particular subject.

It is also found experimentally (*8–10*) that there are differences in the spin relaxation times of various tissues and Kiricuta and Simplaceanu (*8*) have shown that there is quite good correlation between the spin–lattice relaxation time T_1 and water content among the various animal tissues, the longer T_1's being observed in tissues with higher water content. Damadian (*11*) and others (*8–12*) have shown that T_1 is longer in malignant tissue by a factor of about 1.5 to 2.0. Such pathological tissue is also found to contain more water.

It would thus seem from the tissue characteristics that an imaging method based on water content and/or T_1 would easily differentiate between the various tissue types yielding cross-sectional images showing anatomical detail as reflected in the distribution of water throughout the body. Experimental variations of the imaging technique designed to measure T_1 as a function of position throughout the specimen might also be used to enhance image contrast. The spin–spin relaxation time T_2, which also varies with tissue type, might be similarly used, given suitable modification of the imaging method.

IMAGING BY LINE SCANNING

Under Imaging Principles, above, we stressed the various details and properties of spin density projections corresponding to the full two-dimensional density distribution. However, it will be clear from that discussion that if a narrow strip of material at y_0 could be isolated from a thin slice of spin magnetization of thickness Δx, as sketched in Fig. 4, then the spin projection of that strip along the y axis created by the gradient G_z is directly proportional to the spin density $\rho(y_0, z)$, provided Δx and Δy are sufficiently small. Of course, if the sample density does not vary appreciably along the x axis, the slice thickness Δx can be greater.

In the experiments described, specialization to a slice was achieved simply by relying on the receiver coil geometry, which in this case was a flat coil 2.0 cm in diameter (*13*). The apparatus and probe arrangement are described elsewhere (*13–15*). Isolation of the narrow strip of magnetization was achieved by selectively exciting the spins, within the shaded strip of Fig. 4, by applying a tailored 90° rf pulse. By tailoring we mean shaping the pulse such that its frequency components interact with the spins within a narrow range of Larmor frequencies. During this irradiation process only the selection gradient G_y is switched on and it is this which produces the spread in Larmor frequencies. At the

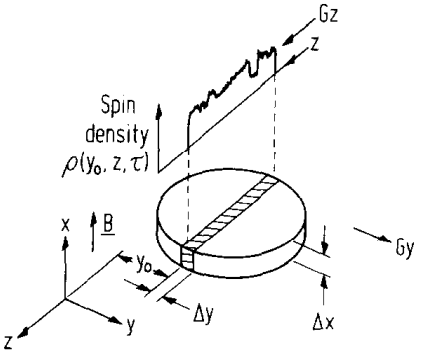

FIG. 4. Illustration of the principle of line scanning. See text for details.

end of the excitation period G_y is quickly switched off and the read gradient G_z is switched on. The FID during the read period is sampled and Fourier transformed to yield one line of the two-dimensional spin image. In the fully automated version of this experiment the rf excitation spectrum is recalculated on-line by a control computer to give a new value of offset y_0 and the process is repeated. In this way the whole imaging field is scanned line by line and the data are formed into a rectangular array in the computer memory. This is then used to modulate the spot intensity in a television-type display (*14*).

In modifications of this kind of experiment, better definition of the slice thickness Δx may be achieved by a further use of selective excitation pulses to define the initial undisturbed slice of magnetization. An even simpler arrangement, based on the first method described above, involves producing a set of two-dimensional pictures by advancing the object to be imaged along the x axis through the receiver coil. A spatial deconvolution of corresponding picture elements along the x axis with the receiver coil's spatial response function will yield the true density variation along the x axis. A deconvolution of this type will in general result in a poor signal/noise ratio but this may be recovered by reconvoluting with a rectangular or other spatial window function corresponding to a finite slice thickness Δx. This procedure may also be combined to advantage with other imaging methods; in particular, the planar and echo planar techniques described in the next section.

We assume that one pulse of selective irradiation destroys the local spin magnetization at coordinates y, z in plane x, but that this recovers exponentially, through a single simple spin–lattice relaxation process in a characteristic time $T_1(y, z)$. The effective spin density $\rho(y, z, \tau)$ measured in this type of image will thus depend on the delay time τ between successive excitation pulses according to the expression

$$\rho(y, z, \tau) = \rho(y, z)\,[1 - e^{-\tau/T_1(y, z)}]. \qquad [6]$$

By adjusting τ so that $\tau/T_1(y, z)$ is small, for example, one can reduce the effective localized spin density, thereby increasing picture contrast. We refer to this as spin–lattice relaxation time discrimination.

By way of an example of the kind of definition and quality that has been achieved by line scanning, we show a recent cross-sectional scan through an okra seed pod (Fig. 5a) which was later cut through and photographed (Fig. 5b) to yield a direct comparison of the visual cross section with that of the NMR image. The y-axis irradiation gradient corresponding to the vertical picture axis was 0.76 G cm^{-1} and the z-axis read gradient (horizontal picture axis) was 1.38 G cm^{-1}. Because of the rather long spin–lattice relaxation times in plants, the delay time must be correspondingly long and, in this case, it was $\tau = 0.73$ sec. Each line of the picture is an average of 100 separate shots and the complete picture took 78 min to produce, including Fourier transformations.

For other examples of our line scans including images of live human fingers, other biological specimens and examples of spin–lattice relaxation time discrimination, we refer the reader to the literature (*15–17*).

PLANAR AND MULTI-PLANAR IMAGING METHODS

Multiple-Line Selective Irradiation

The basic idea embodied in this method rests in the attempt to superimpose a discrete lattice structure on an otherwise continuous spin density distribution (*18, 19*). From the

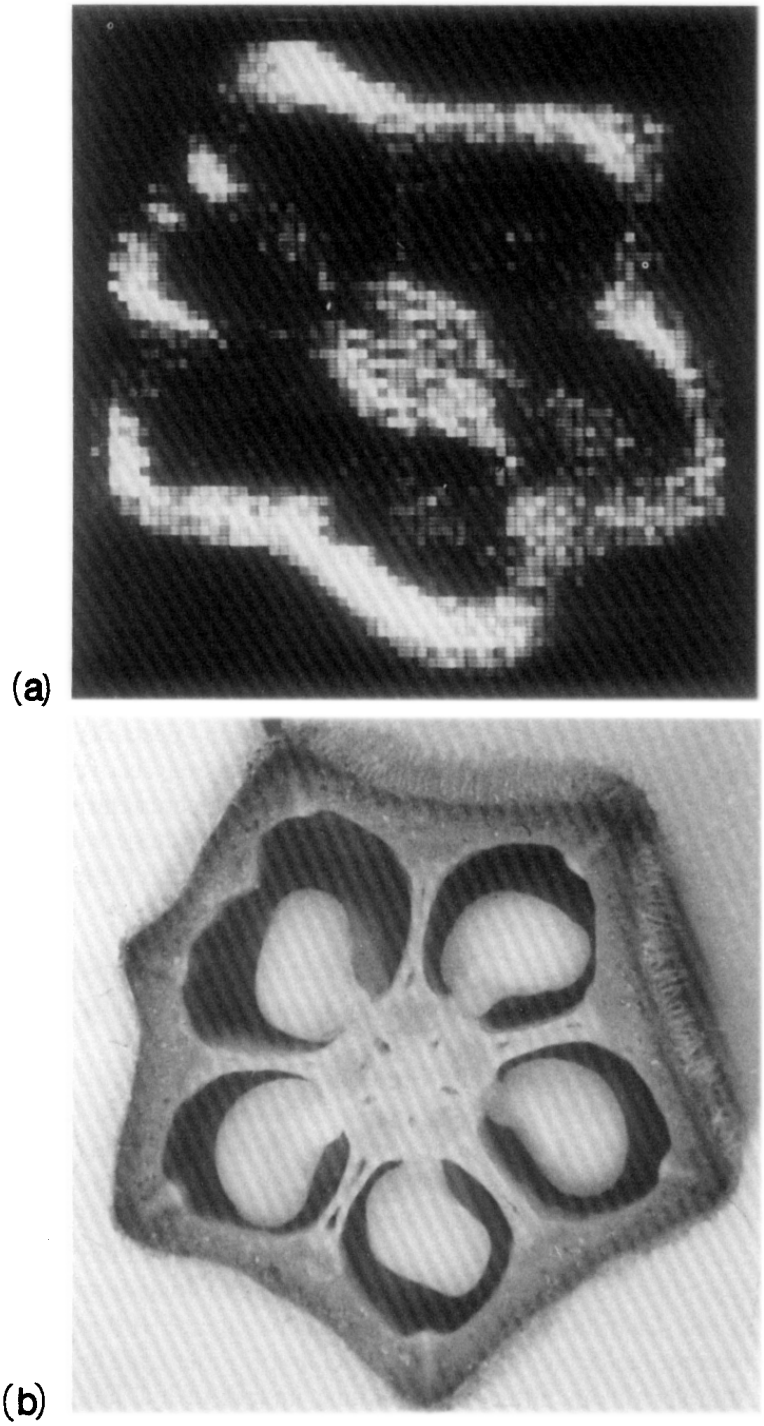

FIG. 5. (a) Line-scan NMR cross-sectional image taken through a whole okra seed pod. (b) Cross-sectional photograph taken through the same region of the pod after the NMR scan.

discussion of discrete lattices under Imaging Principles above, it follows that if such a scheme can be realized in practice a great simplification and speeding up of the imaging process can be achieved, since full two- or three-dimensional information can be simultaneously read out and differentiated in a single FID.

For two-dimensional or planar imaging a gridlike structure of active spins can be superimposed on the specimen simply by selectively irradiating with rf having a uniformly spaced stick spectrum. This is performed with only the initial selection gradient G_y, as in Fig. 4.

Referring to Fig. 6 and using the image of the letter F once more as an illustration, we see that multiple selective excitation (in this case four lines) initially excites the spins falling within the narrow strips of specimen as indicated. In order to differentiate the FIDs from the variously excited lines of spins in the specimen (shaded portion of Fig. 6) the initial selection gradient G_y is kept on together with the read gradient G_z while the FID is sampled during the read phase. The combined gradients produce a projection profile at an intermediate angle as sketched in Fig. 6.

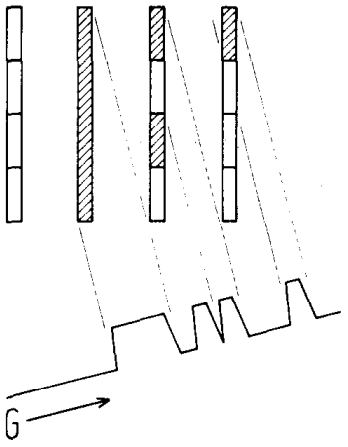

FIG. 6. Principle of planar imaging by the method of multiline irradiation. Intermediate angle projection of the letter F (shaded) through the unirradiated gaps in the image field.

Provided the gradient G_z is chosen according to Eq. [4] so that successive cross-sectional profiles do not overlap, all the information for construction of a two-dimensional picture is contained in a single projection profile in gradient $\mathbf{G} = \mathbf{j}G_y + \mathbf{k}G_2$.

Although there may be spins within the gaps between adjacent strips, these are not excited and hence do not contribute to the profile. Thus, while this method of planar imaging is faster than line scanning, its sensitivity is less than ideal because of the lost spins in the unirradiated gaps. From Fig. 6 it is clear that one must have gaps and although the ratio of gap width to strip width can be reduced to about 4 : 1 it means that at any particular time during the imaging process and even allowing for an interlace procedure, only 25% of the entire sample actually produces signals.

Echo-Planar Imaging

Our predilection with the problem of imposing a discrete lattice structure on an otherwise continuous spin distribution leads us to consider more efficacious methods of achieving this aim. As we have seen, selective irradiation does achieve the desired discreteness, but at the expense of reduced sensitivity.

In Imaging Principles above we were concerned with the determination of periodic structures using Fourier transformation in a continuous time domain. In the method to be described in this section (*20*), we consider what might be regarded as the

complementary situation, namely, the determination of a continuous spin density distribution when periodicity in the time domain is imposed.

As with our previous planar imaging method, the object of this experiment is to produce at high speed cross-sectional NMR images corresponding to the mobile spin density variations throughout a living biological specimen. This speed is imperative if NMR is to be successfully used in medical imaging.

For simplicity we restrict the preliminary discussion of the new method to two-dimensional imaging in one plane. Consider an extended specimen (Fig. 7) placed in a

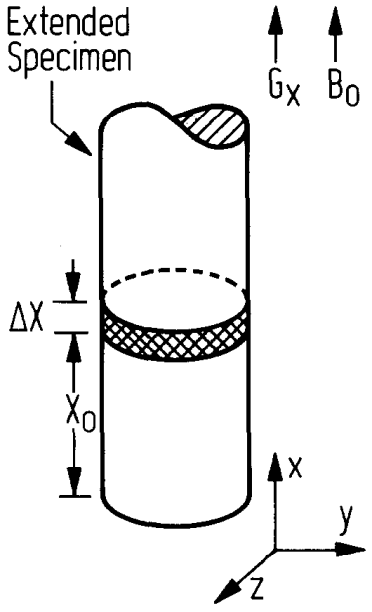

FIG. 7. Selective irradiation of a thin slice of material, thickness Δx, within an extended specimen.

large uniform static magnetic field B_0 which defines the equilibrium spin polarization axis. A linear magnetic field gradient $G_x = \partial B_x/\partial x$ is also applied and at the same time a tailored 90° rf pulse excites the spins within a single slice of thickness Δx *at* x_0, producing an FID. Immediately following this excitation pulse, the gradient G_x is switched off and the FID is observed in a switched gradient $G_y = \partial B_x/\partial y$ and a steady gradient $G_z = \partial B_x/\partial z$. The effect of gradient switching is best understood by first considering the Fourier transform of a periodic function.

Let us consider the damped periodic function, $f(t)$, sketched in Fig. 8a. In an NMR experiment such a signal might be produced in a single field gradient G_y ($G_z = 0$) by recalling the FID, $g(t)$, with a 180° rf pulse at time $(2n + 1)\tau$ following an initial 90° pulse. Alternatively, the gradient G_y can be periodically reversed to produce a series of spin echoes. In either experiment the resulting echoes will decay by a relaxation or a diffusion process in some manner described by the function $h(t)$.

Now in general if the periodic function is described by

$$f(t) = h(t) \sum_{n=0}^{\infty} g(t - 2n\tau), \qquad [7]$$

then the Fourier transform is

$$F(\Omega) = \frac{\pi}{\tau} \sum_{n=-\infty}^{\infty} \left\{ G\left(\frac{n\pi}{\tau}\right) H\left(\Omega - \frac{n\pi}{\tau}\right) \right\}, \quad [8]$$

where the Fourier transforms of $h(t)$ and $g(t)$ are $H(\Omega)$ and $G(\Omega)$, respectively, and the area under $H(\Omega)$ is normalized to unity. An echo train as described by Eq. [7] and the corresponding Fourier transform are illustrated in Figs. 8a and b. If the echoes do not decay significantly, we may take $h(t) = 1$ in which case $H[\Omega - (n\pi/\tau)]$ becomes the

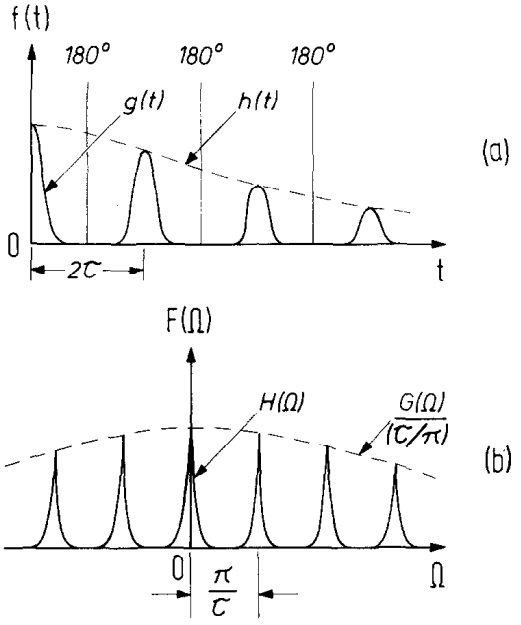

FIG. 8. (a) Periodic function showing an FID followed by a series of damped spin echoes. (b) Fourier transform of complete signal as in (a).

Dirac delta function $\delta[\Omega - (n\pi/\tau)]$. Recalling the signal in this way and sampling the full spin echo train imposes a discreteness on the Fourier-transformed projection profile. The discrete frequency spacing is given by $\Delta\omega = \pi/\tau$.

In the full two-dimensional experiment the switching sequence for which is shown in Fig. 9 for the case of y-gradient reversal, signal sampling is performed with the additional steady gradient G_z which broadens the individual discrete lines to yield, for a single echo train plus Fourier transformation, a complete set of resolved cross-sectional profiles of the spin distribution across the thin layer in the specimen. Figure 10 illustrates how this comes about in the case of a sample in the form of an annulus. The top diagram shows the discrete projection obtained by modulating G_y with $G_z = 0$. The lower projection obtained with both gradients, G_z static, contains all the cross-sectional profiles of the annulus. The profiles can then be appropriately formed into a rectangular array of data points within a computer memory and then output in a television display as described previously.

If 180° rf pulses are used instead of field gradient reversal to produce the spin echoes, then G_z must be periodically reversed. Since this gradient is smaller than G_y, it will be

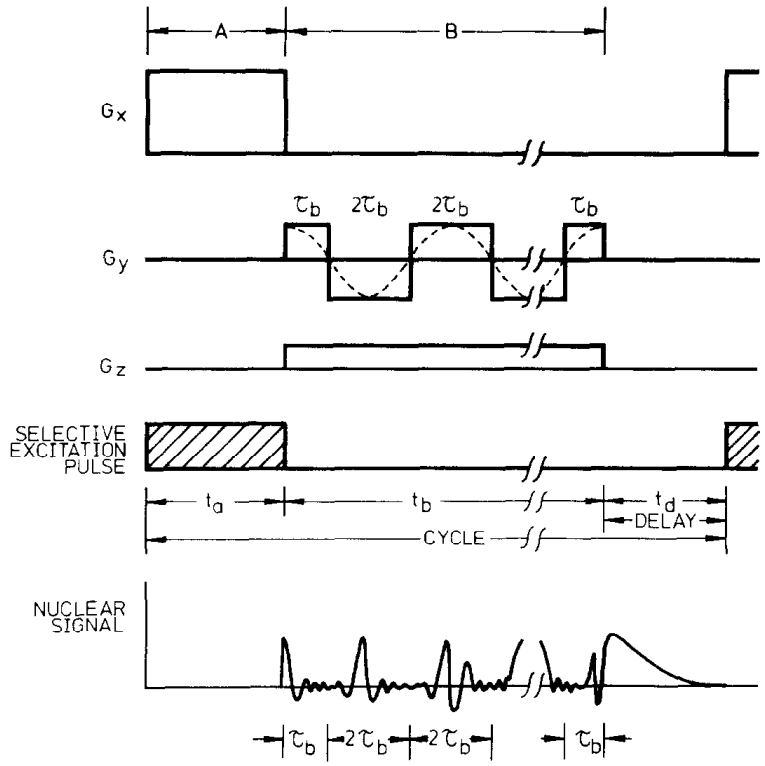

FIG. 9. Pulse and field gradient timing diagram for a two-dimensional echo-planar imaging experiment.

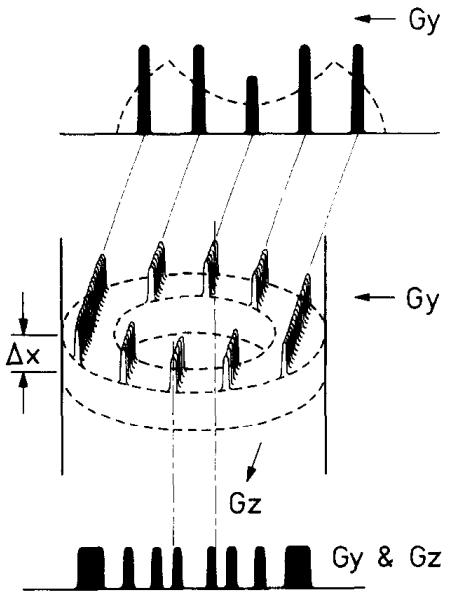

FIG. 10. Spin projections for a homogeneous annulus. The upper projection (dotted) is the projection in G_y alone. This turns into the discrete profile if G_y is modulated. The lower projection corresponds to the application of a modulated G_y gradient together with G_z on continuously. See text and Fig. 9 for further details.

easier in general to accomplish this but the price paid is larger rf pulse amplitudes and therefore a higher mean rf power applied to the sample.

In a generalization of these experiments to three dimensions a multiplanar selection process can be incorporated by modulating both G_x and G_y while maintaining G_z steady (mixed versions of this experiment in which 180° pulses and field gradient switching occur can also be devised as described above). In this case, the initial selective excitation pulse can be replaced by a conventional nonselective 90° (or θ°) rf pulse. As we show in the following analysis, the effect of gradient switching together with digital sampling of the signal is to impose on an otherwise continuous spin density distribution a discrete lattice point distribution with spatial periodicities a, b, and c.

The FID signal in the rotating reference frame at time t following the pulse is given by

$$S(t) = \text{r.p.} \iiint \rho(x, y, z) \exp\left[i\gamma \int_0^t (xG_x(t') + yG_y(t') + zG_z)\, dt'\right] dx\, dy\, dz. \quad [9]$$

We first consider the effect of the time-dependent x gradient alone in Eq. [9] and write the integral over x as a new function $f(y, z, t)$. If $G_x(t)$ is periodic, modulo $2\tau_a$, then we have

$$f(y, z, t) = \int dx \rho(x, y, z) \exp\left[i\gamma \int_0^t xG_x(t')\, dt'\right] \quad [10]$$

$$= \sum_{p=0}^{N} g(y, z, (t - 2p\tau_a)),$$

where we have assumed the damping function $h(t) = 1$ in Eq. [7]. If the modulation is square wave and τ_a is chosen to be long enough for the FID to decay to zero amplitude, then with $G_y = G_z = 0$, Eq. [10] integrated over y and z yields a spin echo train. When all three gradients are applied with appropriate square-wave modulation, we may write the density $\rho(x, y, z)$ as a function of angular frequency $\rho(\omega_x, \omega_y, \omega_z)$. For large even N the Fourier transform of $f(y, z, t)$ becomes therefore

$$F(\omega_x, \omega_y, \omega_z) = \sum_{l=-\infty}^{\infty} 2\pi a \rho(l\Delta\omega_x, \omega_y, \omega_z)\, \delta(\omega_x - l\Delta\omega_x), \quad [11]$$

where $\delta(\omega_x - l\Delta\omega_x)$ is the Dirac delta function.

A similar transformation with respect to the integral over y introduces a second delta function $\delta(\omega_y - m\Delta\omega_y)$. In both delta functions l and m are integers and the angular frequency intervals between points are given by

$$\Delta\omega_x = \pi/\tau_a = \gamma a G_x, \quad [12]$$

etc. The inverse Fourier transform of Eq. [11], when substituted back into Eq. [9] together with the corresponding substitution for the y integrand, yields finally

$$S(t) = \left(\frac{ab}{\gamma G_z}\right) \sum_{l,m} \int d\Omega(l, m) \rho[\Omega(l, m)] \cos \Omega(l, m)t, \quad [13]$$

where the angular frequency $\Omega(l, m)$ is given by

$$\Omega(l, m) = l\Delta\omega_x + m\Delta\omega_y + \omega_z. \quad [14]$$

Digital sampling of $S(t)$ for a time τ_c introduces a discreteness along the z axis. The points are spaced at $z = z_0 + nc$ (n is an integer) which corresponds to an angular frequency interval $\Delta\omega_z = 2\pi/\tau_c = \gamma c G_z$. Taking this into account we may rewrite Eq. [13] as the discrete sum

$$S(t) = \sum \rho_{lmn} \cos t[l\Delta\omega_x + m\Delta\omega_y + n\Delta\omega_z]\, \Delta v_{lmn}, \qquad [15]$$

where $\Delta v_{lmn} = abc$ is the unit cell volume. Thus all spins in each unit cell contribute to the appropriate lattice point. If the modulation periods (and hence the gradients) are chosen so that

$$\Delta\omega_x/M = \Delta\omega_y = N\Delta\omega_z, \qquad [16]$$

where M and N are the largest values of m and n, respectively, in the imaging field, then we see from Eq. [15] that all points in the distribution ρ_{lmn} are uniquely defined in the frequency domain.

Fourier transformation of $S(t)$ in Eq. [15] will thus yield in one calculation the complete three-dimensional spin density distribution function ρ_{lmn}. We refer to this as Fourier transform nesting and in effect it converts a three- (or two-) dimensional transformation to one-dimensional form.

The statement above that all spins in the unit cell contribute to the observed signals means that echo-planar imaging is in principle an efficient method. How this comes about is further clarified.

Looking at the discrete projection profile (top diagram of Fig. 10), the spikes and gaps in the frequency spectrum are created by constructive and destructive interference in the superimposed set of amplitude-modulated continuous spectra with progressively shifted modulation frequencies. It is as if the continuous spectral distribution is squeezed together periodically to create the spikes and gaps, but in such a way as to keep the total area under the discrete curve equal to that of the original continuous curve. For a finite number of echoes, N, the amplitudes of the spikes are just N times that of corresponding points on the continuous spectrum obtained from a single FID. If a discrete profile were produced by the multiple-irradiation method (*18, 19*) in the same time, the spike amplitudes would be equal to corresponding points on the continuous spectrum, thus representing a considerable loss in signal/noise ratio, and hence imaging efficiency.

Provided the conditions on gradient amplitude and periodicity are maintained, it is straightforward to see from Eq. [9] that the square waveforms of the field gradient modulations may be replaced by cosine waveforms to good approximation. For optimum working of this experiment, the gradient modulations must be phase coherent.

If the time-saving gains are to be effective in planar imaging, the complete signal-sampling cycle must be repeated frequently so that data acquisition approaches a continuous process for signal/noise ratio enhancement purposes. The coherent nature of the method described lends itself to the incorporation of complementary store cycles along the lines of the driven equilibrium Fourier transform (DEFT) technique for signal averaging (*21*) or possibly the steady-state free precession (SSFP) technique (*3, 22*), both methods making signal observation essentially independent of spin–lattice relaxation effects if required.

Experimental. Figure 11 shows the first image produced by the echo-planar method. The sample was an oil-filled annulus with outside and inside diameters of 13.8 and 9.3

mm, respectively. The experiment was performed at 15.0 MHz using three field gradients as indicated in Fig. 9 and the image corresponds to a cross-sectional slice of about 4.5-mm thickness and could thus be properly described as a three-dimensional image. The final picture, which is an average of 16 separate shots, took 1.9 sec for the data acquisition and approximately 3 sec for the 1024-point Fourier transform and in the original form comprised 512 separate data points forming a 32 × 16 array. This has been linearly interpolated along the vertical and horizontal picture axes to give a finer grid presentation of the picture of approximately 64^2 elements. The initial selective pulse length $t_a = 7.4$ msec and the y-gradient switching period $2\tau_b$ (in this case square-wave

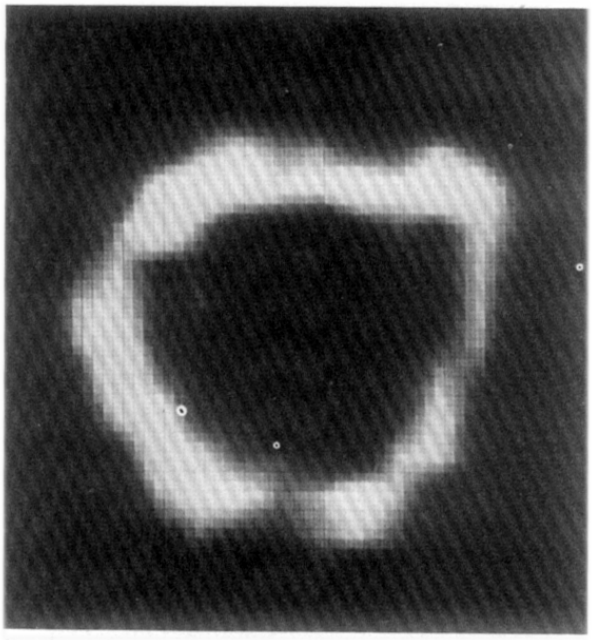

FIG. 11. Echo-planar image of an oil-filled annulus. See text for experimental details.

modulation) was 1.28 msec. The data sampling period was 20 μsec and the total B phase gradient modulation time $t_b = 10.24$ msec. Thus each full unaveraged cross-sectional picture took 17.64 msec to produce in this case. The field gradient values used were $G_x = 0.23$ G cm^{-1}; $G_y = 1.26$ G cm^{-1}, and $G_z = 0.14$ G cm^{-1}. We believe that some of the picture distortion is caused by gradient nonlinearity; however, most seems to be attributable to gradient-switching transients which introduce undesirable phase shifts in the picture data. The data used to produce Fig. 11 have in fact been partially phase corrected, although it is clear from the remaining distortion that a single phase correction as applied here to compensate the right-hand half of the picture is inadequate. The apparatus used for this experiment has been substantially described elsewhere (*13–15*).

TOWARDS WHOLE-BODY IMAGING

The scaling up of one or other of the imaging techniques discussed to allow whole-body imaging of humans is scientifically feasible but introduces certain technical difficulties. The tuning range of transmitter coils large enough to accommodate a human subject will depend on the coil geometry and the desired rf uniformity and will be restricted at the highest tunable frequency to typically 5 or 6 MHz. This is perhaps just

as well since the cost of producing large-volume static magnetic fields in excess of 1 kG becomes inordinately high and suggests a cost limit in operating frequency for protons of about 4.0 MHz. Also, rf penetration of the subject, regarded as a conducting mass, is unlikely to be troublesome at these low frequencies.

In terms of maximum field uniformity for maximum available volume, approximations to spherical magnets seem quite promising. A typical coil arrangement showing one possible disposition of the subject in the field is shown in Fig. 12. Such a coil geometry allows considerable internal space for the probe and gradient coils, but is somewhat sensitive to coil alignment in order to obtain the optimum field uniformity.

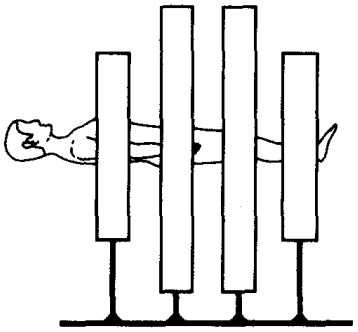

FIG. 12. A four-coil electromagnet for whole-body imaging showing one possible disposition of the subject.

The problem of field gradient switching or modulation on a large scale also poses some difficult technical problems.

Cross-Sectional Water Distributions in Human Subjects

As we have already seen in Fig. 3, there is a significant variation in the amount of water present among many of the different types of human tissue, thus allowing a substantial number to be differentiated according to water content.

Although some tissues are indistinguishable on the basis of water content, if one considers in addition the geometrical location of the organ or region within the living subject, one can expect to observe differentiation and contrast of the morphological detail. This we have already seen in the case of NMR images of live fingers (*15*). It is therefore instructive and useful to use the measured water contents in conjunction with the known geometrical disposition of the internal organs taken from X-ray tomographs or actual anatomical cross sections to produce visual pictures of the water distribution. We have done this for two important examples: (a) a cross section through a human brain, and (b) a whole-body cross section. The brain is taken from a cross-sectional photograph (*23*), and the skull bone and skin have been added. The whole-body distribution is based on the anatomy revealed in a Deltascan X-ray cross-sectional picture (*24*). In producing these cross-sectional water distribution images, we have deliberately divided the image field into a 64^2 array in order to approximate the expected effect in an NMR-produced image.

The full range of water content, that is to say, 0–100%, is in each picture represented by a sixteen-level grey scale, although sixteen separate grey shades are not in fact needed. In both pictures black represents zero water content. In the original pictures,

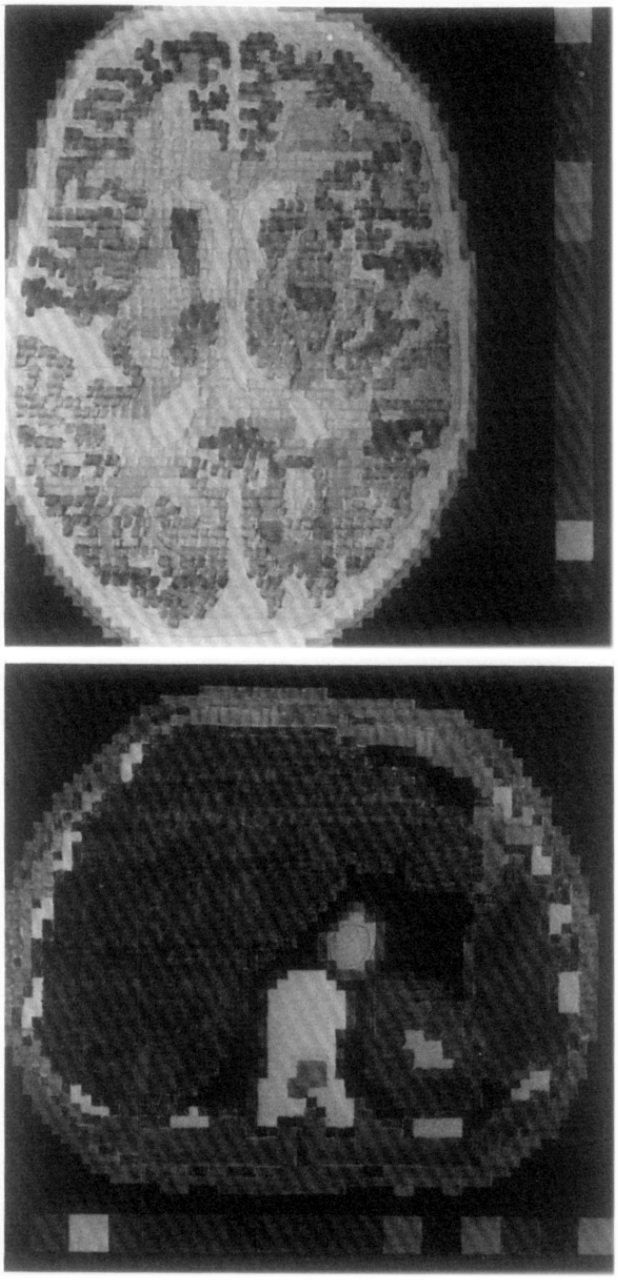

FIG. 13. Hand-produced pictures showing the distribution of water throughout human anatomical sections. (a) Cross section through the head (b) Cross section through the body just below the diaphragm. See text for further details.

which were produced by hand and in colour, the colours in the scale were chosen to give maximum colour contrast among the various tissues and they do not convert to a linear grey scale in the black and white pictures. Nevertheless, the full geometrical detail and differentiation of the internal structures is observable.

The brain image of Fig. 13a clearly demonstrates that differentiation of the grey and white nervous tissue of the cerebral cortex is possible and in spite of the coarseness of the array considerable detail of the convolutions and arachnoid cavity in a normal brain

are to be expected. Perhaps more interesting is the whole-body cross-sectional water image of Fig. 13b, which clearly reveals the liver, one kidney, the spleen, the aorta, and spinal vertebra. The rib sections and upper psoas muscle can also be seen in this picture.

CONCLUSIONS

The ability of NMR imaging to produce cross-sectional medical images of live human fingers which reveal considerable recognizable anatomical detail has already been demonstrated (*15, 17*). We have also shown that cross-sectional NMR images of plants compare rather well with the actual visual cross sections obtained after scanning. All the pictures obtained by a line-scanning method, although of high quality, are somewhat slow to produce. Extension of line scanning to whole-body imaging is therefore unlikely to be of any general medical value because of its relatively low speed, except perhaps in regions of the anatomy where involuntary movement is negligible, for example, the head and limbs.

Much faster methods of imaging have been discussed and in particular, the new method of echo-planar imaging is described which allows all points in a plane or set of planes throughout a subject to be simultaneously recorded and differentiated. Preliminary experimental results for a simple object in the form of a liquid annulus indicate that the method does work as predicted. However, the picture quality so far is rather poor. Nevertheless, anticipating this or a similar method being used for whole body imaging, we can predict that whole-body cross-sectional NMR images will be produced at 4.0 MHz with 10 : 1 signal/noise ratios in a few seconds.

We have anticipated the resolution and quality of such whole-body NMR images by producing cross-sectional water distribution images of the human head and body based on measured water content of various human tissues and morphological detail obtained from X-ray cross-sectional images and cross-sectional anatomical photographs. The water distribution images produced confirm our expectation that water content alone will yield recognizable anatomical images of normal tissue and organs in a subject. Insofar as pathological conditions are known to affect the water balance and distribution in the body, it is expected that such water content maps will aid the detection and diagnosis of disease. This should be particularly useful when such changes in water content are localized to specific organs or regions of tissue as in the case of tumors, edema, hemorrhage, etc.

ACKNOWLEDGMENTS

It is a pleasure to acknowledge the help of the following people who over various periods from 1972 have actively contributed to the development of NMR imaging in our laboratory: A. N. Garroway, P. K. Grannell, T. Baines, A. A. Maudsley, and A. Jasinski. We are also grateful to the Science Research Council for a studentship for I.P. and an equipment grant with which all the small-scale imaging studies have been performed. We also thank the Medical Research Council for current support of the whole-body imaging project. Professor R. E. Coupland's helpful comments on tissue water content are also gratefully acknowledged.

REFERENCES

1. P. MANSFIELD AND P. K. GRANNELL, *J. Phys. C* **6,** L422 (1973); *Phys. Rev. B* **12,** 3618 (1975).
2. P. C. LAUTERBUR, *Nature (London)* **242,** 190 (1973); *Pure Appl. Chem.* **40,** 149 (1974).
3. W. S. HINSHAW, *Phys. Lett. A* **48,** 87 (1974); *J. Appl. Phys.* **47,** 3709 (1976).

4. A. KUMAR, D. WELTI, AND R. R. ERNST, *J. Magn. Resonance* **18,** 69 (1975).
5. R. DAMADIAN, L. MINKOFF, M. GOLDSMITH, M. STANFORD, AND J. KOUTCHER, *Physiol. Chem. Phys.* **8,** 61 (1976).
6. R. GORDON AND G. T. HERMAN, *Commun. Assoc. Comput. Mach.* **14,** 759 (1971).
7. T. F. BUDINGER, "Recent Advances in Nuclear Medicine" (J. H. Lawrence, Ed.), Chap. 2, Grune & Stratton, New York, 1974.
8. I. G. KIRICUTA AND V. SIMPLACEANU, *Cancer Res.* **35,** 1164 (1975).
9. H. E. FREY, R. R. KNISPEL, J. KRUUV, A. R. SHARP, R. T. THOMPSON, AND M. M. PINTAR, *J. Nat. Cancer Inst.* **49,** 903 (1972).
10. D. P. HOLLIS, L. A. SARYAN, J. C. EGGLESTON, AND H. P. MORRIS, *J. Nat. Cancer Inst.* **54,** 1469 (1975).
11. R. DAMADIAN, *Science* **171,** 1151 (1971).
12. I. D. WEISMAN, L. H. BENNETT, L. R. MAXWELL, M. W. WOODS, AND D. BURK, *Science, N.Y.* **178,** 1288 (1972).
13. P. MANSFIELD, A. A. MAUDSLEY, AND T. BAINES, *J. Phys. E.* **9,** 271 (1976).
14. T. BAINES AND P. MANSFIELD, *J. Phys. E.* **9,** 809 (1976).
15. P. MANSFIELD AND A. A. MAUDSLEY, *Brit. J. Radiol.* **50,** 188 (1977).
16. P. MANSFIELD AND A. A. MAUDSLEY, *Phys. Med. Biol.* **21,** 847 (1976).
17. P. MANSFIELD AND A. A. MAUDSLEY, *in* "Proceedings of the 19th Congress Ampere, Heidelberg 1976" (H. Brunner, K. H. Hausser, and D. Schweitzer, Eds.), p. 247.
18. P. MANSFIELD AND A. A. MAUDSLEY, *J. Phys. C* **9,** L409 (1976).
19. P. MANSFIELD AND A. A. MAUDSLEY, *J. Magn. Resonance,* **27,** 101 (1977).
20. P. MANSFIELD, *J. Phys. C* **10,** L55 (1977).
21. E. D. BECKER, J. A. FERRETTI, AND J. C. FARRAR, *J. Amer. Chem. Soc.* **91,** 7784 (1969).
22. H. Y. CARR, *Phys. Rev.* **112,** 1693 (1958).
23. J. AMBROSE, *Brit. J. Radiol.* **46,** 1023 (1973).
24. H. E. JOHNS, *Brit. J. Radiol.* **49,** 745 (1976).